Stand-off detection of solid targets with diffuse reflection spectroscopy using a high-power mid-infrared supercontinuum source

Malay Kumar,[1,*] Mohammed N. Islam,[1,2] Fred L. Terry, Jr.,[1] Michael J. Freeman,[2] Allan Chan,[3] Manickam Neelakandan,[3] and Tariq Manzur[4]

[1]Department of Electrical Engineering and Computer Science, University of Michigan, 1301 Beal Avenue, Ann Arbor, Michigan 48109, USA

[2]Omni Sciences, Inc., 9477 N. Territorial Road, Suite 120, Dexter, Michigan 48130, USA

[3]United States Army CERDEC I2WD, Aberdeen Proving Ground, Maryland 21005, USA

[4]Naval Undersea Warfare Center (NUWC, DIVNPT), 1176 Howell Street, Building #1319, Room #318, Newport, Rhode Island 02841, USA

*Corresponding author: malayk@umich.edu

Received 7 November 2011; accepted 19 December 2011; posted 2 February 2012 (Doc. ID 157700); published 14 May 2012

We measure the diffuse reflection spectrum of solid samples such as explosives (TNT, RDX, PETN), fertilizers (ammonium nitrate, urea), and paints (automotive and military grade) at a stand-off distance of 5 m using a mid-infrared supercontinuum light source with 3.9 W average output power. The output spectrum extends from 750–4300 nm, and it is generated by nonlinear spectral broadening in a 9 m long fluoride fiber pumped by high peak power pulses from a dual-stage erbium-ytterbium fiber amplifier operating at 1543 nm. The samples are distinguished using unique spectral signatures that are attributed to the molecular vibrations of the constituents. Signal-to-noise ratio (SNR) calculations demonstrate the feasibility of increasing the stand-off distance from 5 to ~150 m, with a corresponding drop in SNR from 28 to 10 dB.

OCIS codes: 300.6340, 320.6629.

1. Introduction

We demonstrate the detection of solid targets at a stand-off distance of 5 m with diffuse reflection spectroscopy using a mid-IR supercontinuum (SC) light source. The SC output spectrum extends from 0.75 to 4.3 μm, has a maximum time-average output power of 3.9 W, and is obtained by pumping a 9 m long ZBLAN (ZrF_4-BaF_2-LaF_3-AlF_3-NaF) fluoride fiber with the output of a dual-stage erbium-ytterbium fiber amplifier. The SC source is used to obtain the reflection spectra of a wide range of samples including explosives, fertilizers, and paint coatings. We observe unique spectral fingerprints in the near- and mid-IR wavelength regions of the reflection spectrum and develop a correlation-function-based algorithm to distinguish between the samples. The demonstrated SC light source has excellent beam quality due to the single-mode fiber output, covers multiple atmospheric transmission windows, and is all-fiber integrated with no moving parts or free space optics. Thus, it is well suited for spectroscopy applications in a wide range of fields such as defense, homeland security, remote sensing, and geology.

Diffuse reflection spectroscopy is a widely used technique for both qualitative and quantitative analysis of IR active samples. The most common method

1559-128X/12/152794-14$15.00/0

involves the use of a conventional Fourier transform infrared (FTIR) instrument fitted with an attenuated total reflection or diffuse reflectance measurement accessory [1]. While the above technique covers the entire near-IR to far-IR spectral range of 0.8 to 20 μm, the substance to be analyzed must be confined to the sample chamber of the instrument, thereby limiting its use to offline measurements in a laboratory environment. Recent advances in mid-IR fiber technology have enabled the use of fiber probe accessories for use with FTIR instruments. Fiber-optic reflectance spectroscopy uses fluoride or chalcogenide fiber bundles that enable portable field analysis by allowing the light to be transmitted and collected outside the sample chamber [2,3]. However, poor SNR due to the lamp light source and fiber loss restrict the distance of the sample from the fiber probe tip to a few centimeters.

The need for stand-off detection of samples requires the transition from lamp-based sources to high-power and high-spatial-coherence laser sources. For the detection of gases, lasers with a very low linewidth are ideal due to the narrow spectral absorption features of the gas. The differential absorption light detection and ranging (DIAL) [4] technique uses two laser wavelengths (either discrete or tunable) to measure the concentration of gases at distances of up to a few kilometers. The technique works by measuring the relative difference in the backscattered signal from the two lasers—one that is tuned to the center of an absorption peak, while the other is tuned outside the peak. However, each target gas requires the use of different laser sources in the respective absorption bands or a widely wavelength tunable source, such as an optical parametric amplifier/oscillator.

Remote Raman spectroscopy is a popular technique for identification of solid and liquid samples at stand-off distances. The sample is illuminated with a high-energy pulse from a visible or ultraviolet YAG laser, and the emitted Raman spectrum unique to the sample is detected with a gated charge-coupled device camera. While this technique offers a simple low-complexity design with excellent overall selectivity, some samples are difficult to analyze due to fluorescence caused by the intense pump beam. Another potential drawback is the need for extremely sensitive detection with large collection optics due to the inherent weak nature of the Raman effect. However, the sensitivity can be increased using resonance Raman spectroscopy [5], in which the probe laser wavelength tuned near an electronic transition within the molecule gives rise to significant enhancement of certain Raman lines. Coherent anti-Stokes Raman spectroscopy [6] is another variation to improve sensitivity, though at the cost of a big increase in system complexity. It is based on a nonlinear conversion of three laser beams into a coherent laserlike Raman beam of high intensity in the anti-Stokes wavelength region. Stand-off Raman spectroscopy has successfully been used in the fields of geology, chemical sensing, and explosives detection at distances of up to 470 m [7].

Laser-induced breakdown spectroscopy (LIBS) is another widely used technique for stand-off detection of explosives at distances of up to 50 m [8]. A high-energy laser pulse is used to create a plasma on the sample surface, and the characteristic atomic emission lines of the constituent elements are analyzed to determine the sample composition. However, the high beam intensity required for the breakdown limits the spot size on the sample to a few millimeters and may cause thermal degradation of the samples. While LIBS offers high sensitivity, the selectivity of the technique is reduced due to contamination from atmospheric gases. A different technique, called photofragmentation laser-induced fluorescence (LIF), uses an initial fragmentation of the explosive molecule followed by LIF detection of characteristic fragments [9]. The technique is used to detect the NO molecule and is thus limited to explosives containing the nitro group. Photothermal spectroscopy [10] is another novel method that has been recently shown to detect the presence of explosive residues at a 1 m distance using tunable quantum cascade lasers. As the laser is tuned to the peak of an absorption feature of the sample of interest, a thermal camera is used to measure the rise in temperature of the sample. The limitation of this technique is similar to DIAL; i.e., each sample of interest requires a different laser specifically tuned to the absorption wavelength.

In comparison, our technique uses a spatially coherent beam from a SC laser to measure the diffuse reflection spectra of solid samples. The SC laser combines the advantages of a broad-bandwidth light source, such as a lamp, with that of a conventional monochromatic laser. The 3000 nm wide output spectrum covers multiple fundamental and overtone molecular vibration absorption bands, and it allows the measurement of a wide range of samples. On the other hand, the high output power and single-mode beam quality enable simple stand-off measurements. In particular, we measured the reflection spectra of several samples at a distance of 5 m and show the feasibility of extending the range to ~150 m using SNR calculations. The reflection spectra obtained using our technique show good agreement with those reported in the literature using conventional methods such as an FTIR or a spectrophotometer.

This paper is organized as follows. Section 2 describes the experimental setup for stand-off reflection spectroscopy, as well as the details of the mid-IR SC laser used for the experiments. In Section 3 we describe the experimental results obtained with three different sample sets. The first set consists of 4%–8% explosives deposited on fused silica crystals, and the second set consists of miscellaneous samples such as ammonium nitrate, urea, gypsum, and pine wood. The third set consists of aluminum blocks painted with different automotive and military paints. The repeatability of the reflectance measurements and comparison of the stand-off spectra with

that obtained using an FTIR instrument are also described in this section. Section 4 describes a correlation algorithm for distinguishing between the different samples on the basis of their unique reflection spectra. The various performance metrics of the system, their limitations, and scope for further improvement are discussed in Section 5. Finally, we summarize the results in Section 6.

2. Experimental Setup

A. Stand-Off Detection Using Diffuse Reflectance Spectroscopy

The experimental setup for a reflection-spectroscopy-based stand-off detection system is shown in Fig. 1, while details about the SC light source are described later in Subsection 2.B. First, the diverging SC output from the ZBLAN fiber is collimated to a 1 cm diameter beam using a 25 mm focal length, 90° off-axis, gold-coated, parabolic mirror. To reduce the effects of chromatic aberration, refractive optics are avoided in the setup. All focusing and collimation are done using metallic mirrors that have almost constant reflectivity and a focal length over the entire SC output spectrum. The sample is kept at a distance of 5 m from the collimating mirror, which corresponds to a total round-trip path length of 10 m before reaching the collection optics. A 12 cm diameter silver-coated concave mirror with a 75 cm focal length is kept 20 cm to the side of the collimation mirror. The mirror is used to collect a fraction of the diffusely reflected light from the sample and focus it into the input slit of a monochromator. Thus, the beam is incident normally on the sample, but detected at a reflection angle of $\tan^{-1}(0.2/5) \sim 2.3°$. Appropriate long wavelength pass filters mounted in a motorized rotating filter wheel are placed in the beam path before the input slit to avoid contribution from higher wavelength orders from the grating (300 groves/mm, 2 μm blaze). The output slit width is set to 2 mm, corresponding to a spectral resolution of 10.8 nm, and the light is detected by a 2 mm × 2 mm liquid-nitrogen-cooled (77 K) indium antimonide (InSb) detector. The detected output is amplified using a transimpedance preamplifier with a gain of

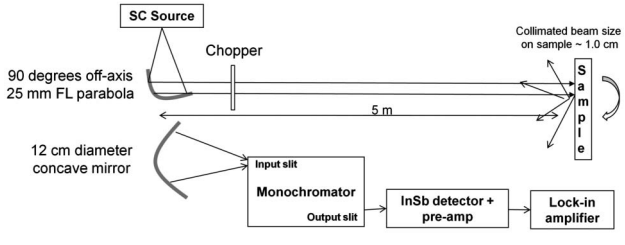

Fig. 1. Experimental setup for SC-based stand-off diffuse reflection spectroscopy. Collimated light from the SC source is incident normally on the sample 5 m away, and diffusely reflected light at a reflection angle of 2.3° is collected by a concave mirror. Low noise detection of the signal is achieved with a lock-in amplifier connected to a liquid-nitrogen-cooled InSb detector at the monochromator output.

$\sim 10^5$ V/A and connected to a lock-in amplifier setup for high sensitivity detection. The use of a chopper and lock-in amplifier enables low noise detection by reducing the noise bandwidth in the measurement. In our experiment, the chopper frequency is set to 400 Hz and the lock-in time constant is set to 100 ms corresponding to a noise bandwidth of ~1 Hz.

The reflection spectrum of a given sample is obtained using the following procedure. First, a reference scan is obtained using an "Infragold" diffuse reflectance target as the sample. Infragold from Labsphere, Inc., is an electrochemically plated diffuse gold metallic coating that has >95% reflectivity from 1 to 20 μm, and a nearly ideal Lambertian scattering profile. Although the SC short wavelength edge is 750 nm, the scans we obtain start at 1200 nm due to the rapid fall-off of the grating efficiency as well as detector responsivity at shorter wavelengths. The scan from 1200 to 4200 nm is comprised of three different scans, each with a different long-pass filter rotated into place via a circular stepper motor. A silicon filter (1100 nm long pass) is used to scan from 1200 to 2100 nm, a germanium filter (1800 nm long pass) to scan from 1800 to 3400 nm, and a 3000 nm long pass filter to scan from 3100–4200 nm. The three different sections are then stitched together using the overlap regions to form a single continuous scan from 1200 to 4200 nm. Despite the use of three long-pass filters in conjunction with a stitching algorithm, we obtain highly reproducible spectra for each measurement. The time taken for the complete scan is about 150 s and is limited by the scanning monochromator. A more detailed discussion regarding the acquisition time is contained in Subsection 5.D.

After obtaining a reference scan, the Infragold target is replaced with the sample of interest, and a second scan is obtained using the same procedure described above. Because the beam passes through the same optics in each case, the wavelength dependence of the system due to the SC shape, detector response, and grating response is identical for both the reference and sample scans. Thus, dividing the sample scan by the reference scan gives the reflectance spectrum of the sample normalized to a Lambertian reflector kept at the same distance. Some samples cannot be oriented in the vertical plane normal to the collimated SC beam due to their powdered nature. To solve this problem, a fold mirror inclined at 45° is added close to the sample to bend the beam 90° and allow the sample to be placed horizontally on the table.

After the reference and sample scans are acquired, postprocessing of the data is performed in MATLAB. The percentage sample reflectance is obtained by dividing the sample scan by the Infragold reference scan, followed by smoothening of the reflectance curve using a five-point Savitzky–Golay filter [11]. Finally, the three outlier data points at 1530, 1540, and 1550 nm are deleted from the final reflectance curve due to the saturation of the lock-in amplifier

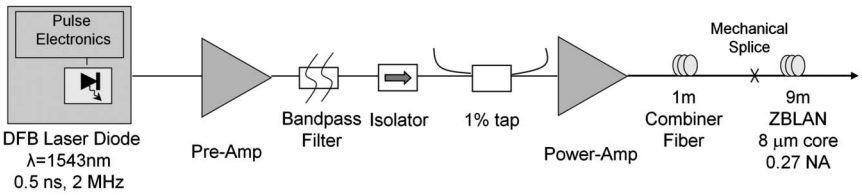

Fig. 2. Experimental setup for mid-IR SC generation in ZBLAN fiber. Light from a 1543 nm telecom laser diode is amplified to ~19 kW peak power in two stages of cladding pumped erbium-ytterbium fiber amplifiers. The output is mechanically coupled into an 8 μm core diameter and 9 m long ZBLAN fiber to produce a broadband SC spectrum.

signal level close to the seed laser wavelength of 1543 nm. For certain samples, the reflectance curve is transformed to a pseudoabsorbance curve using the transformation $A = \log(1/R)$ for better visualization of the features of interest.

B. Mid-IR SC Generation in ZBLAN Fiber

A block diagram of the mid-IR SC source used for the above experiments is shown in Fig. 2. First, a pulse generator is used to produce 0.5 ns pulses at a 2 MHz repetition rate from a 1543 nm distributed feedback (DFB) seed laser diode. Next, the light is amplified to a peak power of ~19 kW using dual-stage cladding pumped Er-Yb fiber amplifiers, pumped by high-power 976 nm laser diodes. A 0.8 nm wide narrowband filter centered at the seed wavelength is placed between the two gain stages to remove the out-of-band amplified spontaneous emission from the preamplifier stage. To prevent heat-induced damage to the power amplifier, the gain fiber is cooled by wrapping it in a spiral groove machined on a cylindrical-shaped copper heat sink. In addition, the entire system is modulated at 500 Hz with a 50% duty cycle to further reduce the thermal load. At the highest 976 nm pump power of 52 W (104 W without modulation), the 1543 nm signal output from the power amp is 9.6 W, corresponding to a pump-to-signal efficiency of 18.5%. Finally, the output from the power-amp is coupled into a 9 m ZBLAN fiber (8/125 μm, 0.27 NA) via a mechanical fiber alignment stage. Because both the output of the power amp and the input of the ZBLAN fiber are angle-cleaved to reduce back reflections, alignment of the two fibers is done under a microscope to ensure the correct rotational orientation of the fiber ends for maximum coupling.

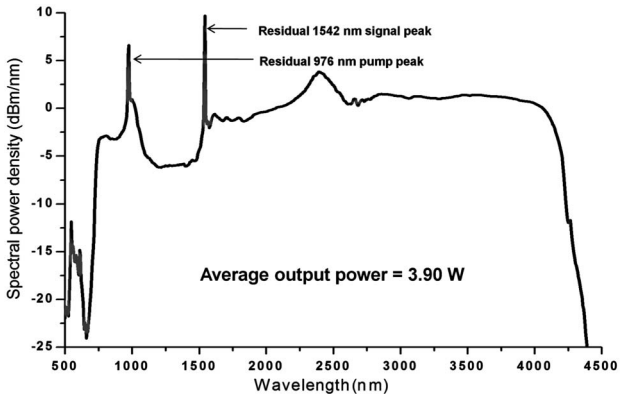

Fig. 3. SC output from 9 m ZBLAN fiber: spectrum spanning 750–4300 nm with 3.9 W average output power. Output has >1 mW/nm (0 dBm/nm) spectral power density in the wavelength range from 2000 to 4200 nm. The broad SC is generated by a mixture of nonlinear effects such as modulation instability and stimulated Raman scattering.

At the output of the ZBLAN, we measure 3.9 W of average output power (with a 50% duty cycle modulation) and a SC spectrum extending from 750–4300 nm (Fig. 3) at the −20 dB level. The output spectrum from 750 to 1750 nm is measured using a calibrated optical spectrum analyzer, while the spectrum from 1200 to 4300 nm is measured using a monochromator setup described in Subsection 2.A. The latter is corrected for both the detector and grating response and then stitched together with the short wavelength spectrum to obtain a continuous curve from 750 to 4300 nm. Finally, the y axis is converted to an absolute scale representing the SC spectral power density in dBm/nm (mW/nm) by scaling the spectrum to ensure that the area under the curve represents the measured average power. Table 1 shows the power in different wavelength bands of the SC measured by using appropriate long wavelength pass (LP) filters and a powermeter. Because the entire SC output is modulated with a 50% duty cycle, the average power during the on time is 2× the values listed in the table. The broad SC is generated by an interplay of nonlinear effects, such as modulation instability and stimulated Raman scattering, while the long wavelength edge is limited by the inherent material absorption loss of the ZBLAN glass [12].

A unique feature of the SC system is the ability to scale the average output power, while maintaining the same spectral shape and, hence, the same

Table 1. Supercontinuum Output Power in Different Spectral Regions[a]

Output	Power
Pump power (976 nm)	52.0 W
Power amp output (1543 nm)	9.6 W
ZBLAN output (entire SC)	3.9 W
1800 nm LP	2.7 W
2500 nm LP	2.0 W
3000 nm LP	1.3 W
3500 nm LP	0.7 W
3800 nm LP	0.5 W

[a]The values are measured using a powermeter and long-pass filters. Because the SC output is modulated with a 50% duty cycle pattern, the average power during the on time of the SC is 2× the values listed in the table.

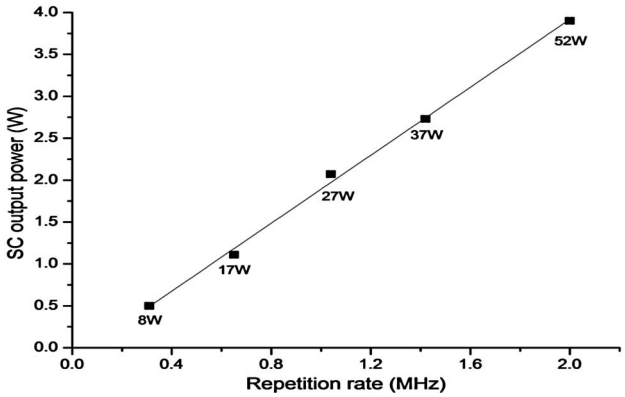

Fig. 4. Power scalability of SC output power. The plot shows a linear increase in SC average output power with the seed laser pulse repetition rate. The corresponding 976 nm pump power used in the power amp stage is listed next to the data points. The SC was operated at the highest repetition rate of 2 MHz for all the sample measurements.

fractional distribution of power in different wavelength bands. We accomplish this by increasing the repetition rate of our seed laser along with a proportional increase in the 976 nm pump power, while maintaining a constant peak power going into the ZBLAN fiber [13]. Figure 4 shows the linear increase in the SC average output power with an increase in the seed laser repetition rate, with the corresponding 976 nm power amp pump power labeled next to the data point. The results shown in Fig. 3 and Table 1 correspond to our highest power results obtained at the 2 MHz repetition rate and 52 W pump power. A further increase in output power was limited by the available pump power, and we expect the results to scale up with higher pump power and thermal management of the critical splice points and power amp gain fiber.

C. Sample Preparation

Three sets of solid samples are chosen to demonstrate the stand-off diffuse reflection spectra measurement capability of our system. The first set consists of "Non-Hazardous Explosives for Security Training and Testing" (NESTT) manufactured by the XM Division of VanAken International. These samples contain small amounts of explosives deposited on an inert fused silica powder substrate. The resulting products are nonflammable, shock-insensitive, and easily transportable, while retaining the unique chemical signature of the explosive that makes them detectable. NESTT samples have previously been used as substitutes for pure explosives in stand-off optical detection using Raman spectroscopy [14]. In our experiments, we use the following samples—trinitrotoluene (TNT), research department explosive (RDX), pentaerythritol tetranitrate (PETN), and potassium nitrate. The TNT, RDX, and potassium nitrate NESTT samples have 8% (by weight) explosives, while the PETN sample has 4%.

The second sample set consists of ammonium nitrate, urea, gypsum, and pine wood. Ammonium nitrate and urea are common fertilizers, but are also often used as explosives. These samples are ground to a fine powder in a mortar and pestle and filled to a depth of ~5 mm in a shallow glass container. We also measure the reflection spectrum of a 10 cm diameter ×0.5 cm thick gypsum ($CaSO_4.2H_2O$) disk and a 5 cm × 5 cm × 0.5 cm piece of pine wood, because these samples are relevant in the remote sensing community (minerals and vegetation).

The final set of samples is selected to distinguish between commercial automotive and military vehicle paints based on their reflection signatures. We obtained red, black, and green acrylic-based spray paints from an auto supply store and sprayed three coats on different areas of a sanded aluminum block to make our automotive paint samples. The sample of the military paint consisted of an aluminum block coated with a chemical agent resistant coating (CARC) green paint, and was loaned to us by General Dynamics—Advanced Information Systems (Ypsilanti, Mich.).

3. Experimental Results

A. Sample Set #1—NESTT—TNT, RDX, PETN, Potassium Nitrate

The chemical structure and molecular formula of the four NESTT samples are shown in Fig. 5, while the absorbance spectra obtained using our SC source are shown in Fig. 6. For each sample, the positions of the strongest/unique peaks have been labeled for clarity, and they are in good agreement with FTIR measurements reported in the literature [15–17]. The common broad absorption feature around 2720 nm present in all four samples arises due to the O–H stretching vibration of hydroxyl groups from absorbed water in the fused silica host.

TNT belongs to a class of compounds known as nitroaromatics, in which the carbon directly attached to the nitro (NO_2) group is part of an aromatic ring. The strongest peaks in the spectrum observed at 3230 and 3270 nm are due to the fundamental C–H stretching vibrations in the aromatic ring. The remaining peaks from 3300 to 3500 nm are also due to the C–H stretch, but from the alkyl group. We also observe sharp but weak features between 2200 and 2600 nm, which arise due to the combination between the C–H stretch and C–H bend vibrations. Finally, the features between 3600 and 3850 nm are

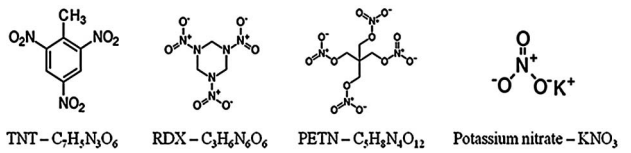

Fig. 5. Chemical structure and formula of NESTT samples—TNT, RDX, PETN, potassium nitrate. TNT belongs to the nitroaromatics class, RDX to nitramines, and PETN to nitrate esters. The fundamental and overtone vibrations of different functional groups are responsible for the unique spectral features observed in each sample.

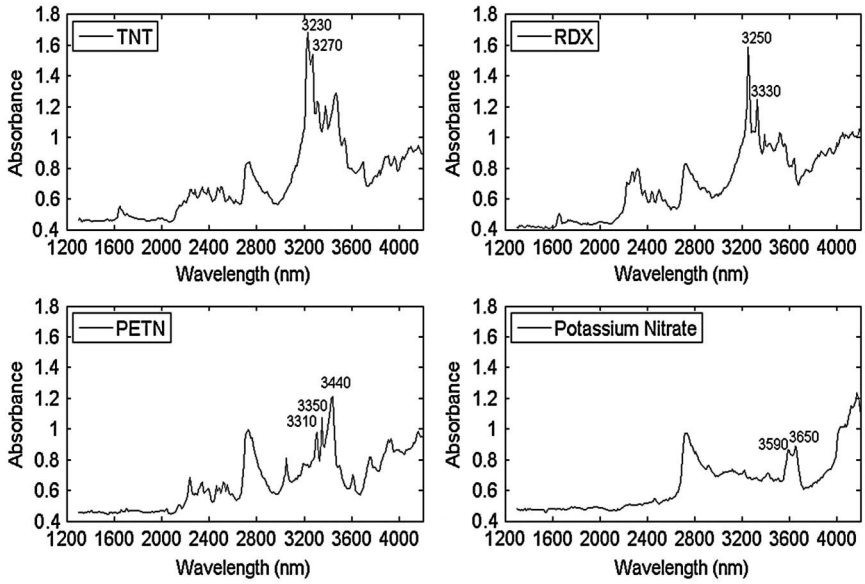

Fig. 6. Absorbance spectra of NESTT sample set #1—TNT, RDX, PETN, potassium nitrate. The strongest absorption features in TNT, RDX, and PETN are in the 3200–2500 nm band and arise due to the fundamental aromatic and aliphatic C–H stretch. The spectral features around 3600 nm in potassium nitrate arise due to the first overtone of the N–O asymmetric stretch. The common broad feature at 2720 nm in all four samples is due to the O–H stretch from absorbed water in the fused silica host.

due to the first overtone of the nitro group symmetric stretch.

RDX belongs to the nitramines class containing the N–NO_2 bond and also has multiple features in the 3200–3500 nm band due to the C–H stretch vibrations. The two strongest peaks in this region are at 3250 and 3330 nm. The spectrum also contains the C–H combination bands from 2200 to 2600 nm and very weak nitro group overtones from 3600 to 3850 nm.

PETN is classified as a nitrate ester containing the C–O–NO_2 bond, and its reflection spectrum is characterized by a triplet of peaks at 3310, 3350, and 3440 nm due to the C–H stretch vibration from the aliphatic groups. The C–H combination band is also present from 2200 to 2600 nm, while the peak around 3900 nm corresponds to the first overtone of symmetric stretching vibration of the O–NO_2 bond. We will show later in Section 4 that the bands from 3200 to 3500 nm and 2200 to 2600 nm will be used to distinguish between the three explosive samples due to the unique positions and shapes of various peaks.

Potassium nitrate, being an inorganic compound, does not contain any absorption features due to the C–H bond present in the other three samples. Instead, the unique spectral feature for this sample is a pair of peaks at 3590 and 3650 nm, which arise due to the first overtone of the asymmetric N–O stretching vibration of the nitrate ion (NO_3).

B. Sample Set #2—Gypsum, Pine Wood, Ammonium Nitrate and Urea

The reflection spectrum for the four samples is shown in Fig. 7. While the absorption features show up as peaks in the absorbance spectrum, they are present as valleys in the reflection spectrum. The predominant spectral features in the gypsum ($CaSO_4.2H_2O$) reflectance occur due to the fundamental as well as combination bands of the water molecule, and the locations are consistent with previously reported values [18]. These valleys are present at 1450, 1750, 1940, and 2860 nm. In addition to the features from water, we also observe small dips in the spectrum at 2220, 2260, and 2480 nm, which arise due to the first overtone of the S–O bending vibration. Finally, the valley at 3970 nm occurs due to the first overtone of the —O–S–O stretching vibration of the sulfate (SO_4^{2-}) ion.

The pine wood spectrum comprises bands due to its main constituents—cellulose, lignin, and water. Poli *et al.* [19] used fiber-optic reflectance spectroscopy to obtain the reflection spectrum of wood and identify the peak assignments. As is the case in the gypsum reflection spectrum, the valleys at 1450, 1920, and 2860 nm are attributed to water. The dip at 2100 nm is due to the first overtone of the C–O asymmetric stretch, the one at 2270 nm is due to the combination band of O–H and C–H, and the one at 2490 nm is due to the combination band of C–H and C–O. Finally, the broad feature around 3450 nm is due to the C–H stretching vibration.

The ammonium nitrate (NH_4NO_3) spectrum has three prominent features in the near-IR region, which were also observed by Canal *et al.* [20] using a halogen light source. The dip at 1270 nm is due to the combination of N–H stretching and N–H bending vibrations, while the dip at 1570 nm is due to the first overtone of N–H stretch. The doublet at 2050 and 2140 nm are possibly due to the second overtone of the N–H bending vibrations, while the fundamental N–H stretch appears as a broad feature around 3000 nm.

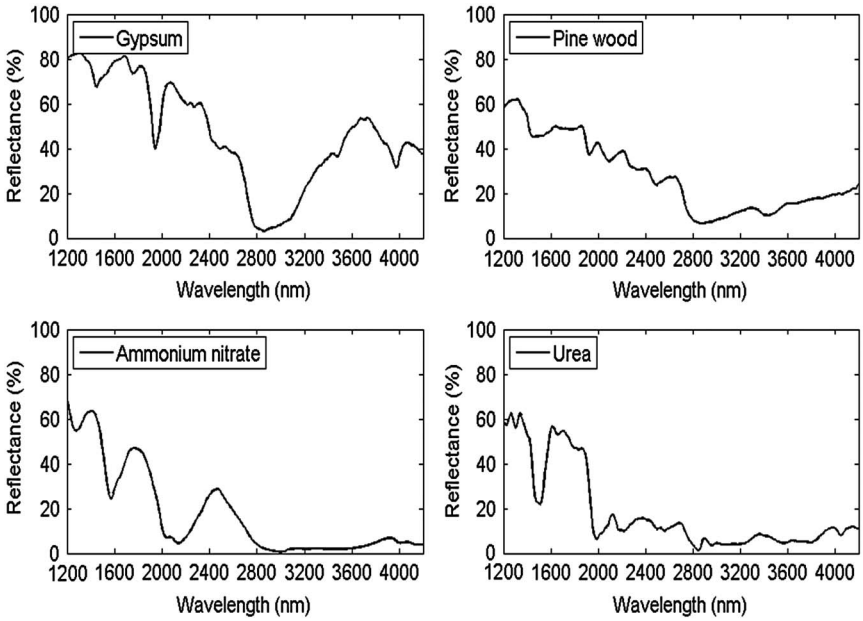

Fig. 7. Reflection spectra of sample set #2—gypsym, pine wood, ammonium nitrate, urea. The main spectral features in gypsum arise due to fundamental and combination bands of water. The pine wood spectrum has absorption features from C–H, O–H, and C–O stretches attributed to cellulose, lignin, and water. The N–H stretch and N–H bending vibrations are responsible for absorption dips in ammonium nitrate, while the C–O stretch produces absorption features in urea.

Urea $(NH_2)_2CO$ has two amide (—NH_2) groups joined by a carbonyl (C═O) functional group. The absorption line at 1490 nm occurs due to the third overtone of the C═O stretching vibration, while the line at 1990 nm is due to the second overtone of the same [21].

C. Sample Set #3—Automotive and Military Paints

In our final set of samples, the objective is to distinguish between commercial automotive paints and military-grade CARC paint based on the differences in their reflection spectra. The obtained reflection spectra of the three automotive and one military paint samples are shown in Fig. 8. Unlike the previous sample sets, the paints consist of a complex mixture of many different chemicals, and, hence, it is not possible to identify individual absorption lines. However, we can make some broad observations regarding the spectral features of the paints.

The difference in reflectance levels of the four paints can primarily be attributed to the surface finish of the paint coats. While the auto-red has a glossy finish, the auto-green, auto-black, and CARC-green paints have a more matte finish. Because our reflection measurement is performed at an angle of only 2.3° away from the specular direction, we expect a higher reflection from the glossy paint. It is important to note that we expect different reflectance levels for the same sample with a different surface finish and at different measurement angles. Thus, in Section 4, we will demonstrate a sample identification algorithm that is only sensitive to the shape and feature positions of the spectrum and not the absolute reflectance level.

Because all four paints contain a variety of organic compounds, we observe strong features between 3200 and 3500 nm from the C–H stretch and from 2200 to 2600 nm due to the C–H stretch and C–H bend combination band. In addition, the 2850 to 3150 nm band in automotive red and green paints has absorption features due to the N–H stretch from the acrylic-melamine base. However, the primary difference between the automotive and CARC paint is the presence of a strong dip between 1200 and 1850 nm in the latter. Using the Lawrence Berkeley National Laboratory Pigment Database [22], we found out that the above feature could be attributed to the absorption from Cobalt Chromite—a green pigment found in CARC-green. The measured spectrum of CARC-green is in good agreement with that reported in the literature [23]. While the features due to Cobalt Chromite were the main difference between the paints in our small sample set, the above green pigment might not work well as a universal discriminator between all military and automotive paints. A more detailed study with a much larger sample set is required to determine the optimum wavelength bands for distinguishing between the two types of paints.

D. Repeatability of Reflection Measurements

The repeatability of the sample reflectance measurements is directly related to the amplitude stability of the SC source. We measure the magnitude of the SC fluctuations by directly coupling the SC output to the monochromator input, and recording the output versus time for a given wavelength. The lock-in amplifier time constant is kept at 100 ms (the

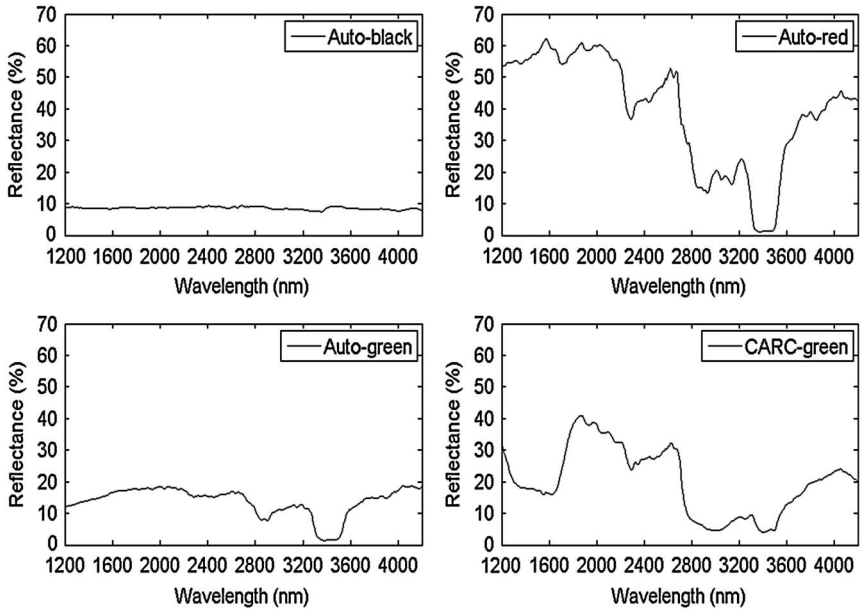

Fig. 8. Reflection spectra of sample set #3—automotive and military CARC paints. The strong absorption from 3200 to 3500 nm in all paints is due to the C–H stretch, while that from 2850 to 3150 nm in the auto-red and auto-green is due to the N–H stretch from the acrylic-melamine base. The unique feature of the CARC-green paint is a broad absorption between 1200 and 1850 nm due to the green pigment Cobalt Chromite.

same value as the setup for sample measurements) and corresponds to an effective noise bandwidth of ~1 Hz. Figure 9 shows the variation of the SC output at 4000 nm over a time period of 300 s. The plot has been normalized to a mean of 100%, and we obtain a standard deviation of 0.16%. While the plot is shown for a wavelength of 4000 nm, we obtain similar values across the entire SC spectrum. Next, the laser is attenuated by 10 dB using a neutral density filter and the experiment is repeated. We find that the standard deviation is almost identical to the previous case, confirming that the SC fluctuations can be modeled as a fixed root-mean-square percentage fluctuation superimposed on the mean SC signal level.

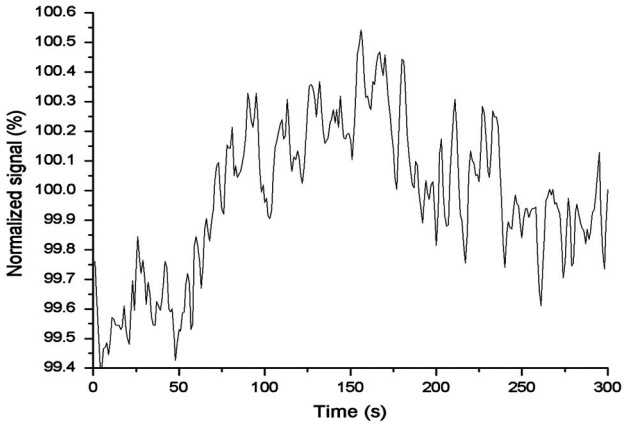

Fig. 9. Variation of SC output at 4000 nm over 300 s. With the signal normalized to a mean of 100%, we obtain a standard deviation of 0.16%. The standard deviation remains unchanged even when the signal is attenuated by 10 dB. Thus, the SC fluctuations can always be expressed as a fixed root-mean-square percentage of the mean SC output, regardless of the absolute signal level.

Thus, the error bar on the reflectance measurements can be equated to the percentage standard deviation (root mean square error) of the normalized SC output.

E. Comparison of SC and FTIR Measurements

In order to verify the validity of our measurements, we compared the reflection spectrum obtained using our setup with that obtained using a diffuse reflectance accessory in an FTIR spectrometer. As an example, Fig. 10 shows a comparison of the powdered urea reflection spectrum obtained using the two methods. There is good agreement in the shape and wavelength position of the various spectral features. However, there is a difference in the absolute reflectance levels of the two curves. We attribute the difference in scale to the different measurement geometries of the two setups. The SC-based setup described in Subsection 2.A measures the reflection spectrum of the sample at a fixed angle of 2.3° from the normal. However, the FTIR accessory uses a concave mirror that collects light over almost the entire hemisphere above the sample. Thus, the latter method produces a directionally integrated spectrum, compared to a single direction spectrum from the former. The shape and positions of the absorption lines depend mostly on the chemical composition of the sample, and hence do not change significantly between the two methods. However, the magnitude of light reflected along different directions depends on the sample texture and, thus, is responsible for the scale difference between the two spectra.

4. Sample Identification Algorithm

This section describes an algorithm that demonstrates the selectivity of our technique, i.e., the ability

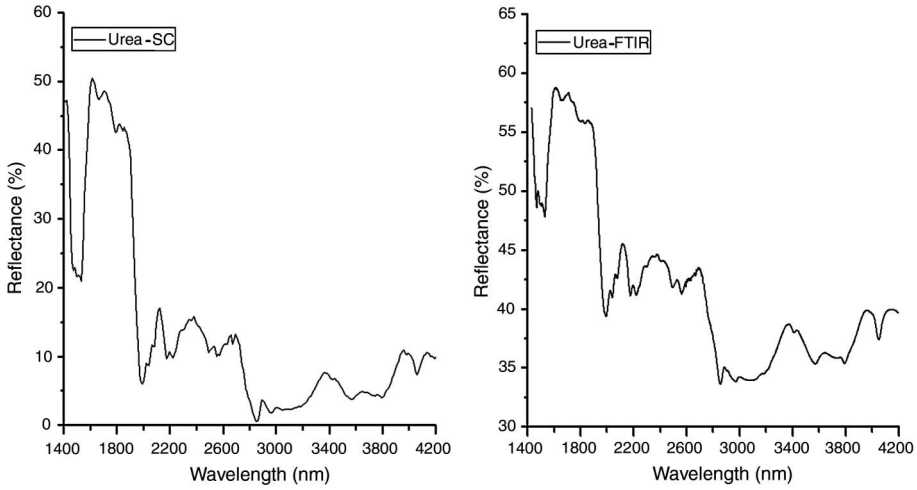

Fig. 10. Comparison of urea reflection spectrum obtained using the SC-based setup with that obtained using an FTIR with a diffuse reflection accessory. There is good agreement in the shape and peak positions of the two spectra. The difference in absolute scale between the two plots is attributed to the difference in reflection measurement geometries of the two setups.

to distinguish one sample from another based on the unique spectral features of each sample. As an extension, the algorithm can also be used to identify an unknown sample by comparing it against a precompiled library of relevant samples. A flow chart describing the different steps of the algorithm is shown in Fig. 11.

Pearson's correlation coefficient r always lies between -1 and 1, with 1 indicating perfect positive correlation and -1 indicating perfect negative correlation. The value of r is independently calculated for each selected wavelength band using the following equation:

$$r = \frac{\sum_{i=1}^{n}(X_i - \overline{X})(Y_i - \overline{Y})}{\sqrt{\sum_{i=1}^{n}(X_i - \overline{X})^2}\sqrt{\sum_{i=1}^{n}(Y_i - \overline{Y})^2}}.$$

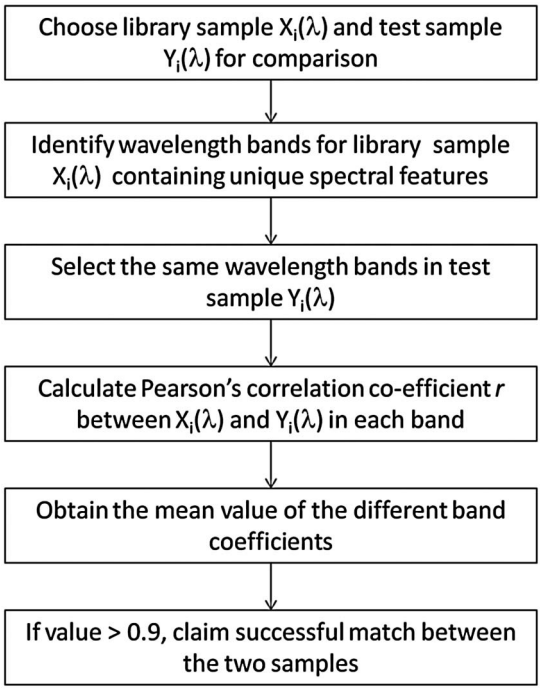

Fig. 11. Flow chart describing the algorithm to demonstrate selectivity between two samples. The algorithm uses the correlation coefficient in selected spectral bands to quantify the degree of similarity or dissimilarity between two reflection spectra. If the mean correlation coefficient over the selected bands >0.9, the two samples are said to be a match.

We test the above algorithm on each of the three sample sets. For each sample in a given set, one or two wavelength bands containing a unique spectral signature are chosen. Tables 2, 3, and 4 show the results of the correlation between different samples in sample set #1, #2, and #3, respectively. As expected, all the diagonal elements of the tables are equal to 1 (the definition of autocorrelation), while the others are below 0.9, thus confirming the ability to distinguish different samples within a set. Table 3 only contains a single row for CARC paint, as the objective was to distinguish the military paint from the automotive paints and not the difference between the different color automotive paints themselves.

The advantage of the correlation-based algorithm we have chosen is the insensitivity to the absolute level of the sample reflectance. The correlation value only depends on the shape and position of the spectral features, and it can be used to compare samples measured using different reflection geometries, as mentioned in Subsection 3.E. While the above algorithm demonstrates proof of concept for distinguishing between distinct samples using multiple wavelength bands, more sophisticated algorithms [24] have been used by the remote sensing community for distinguishing between geological samples with similar compositions. In addition to the detection of pure samples, algorithms using derivative spectroscopy [25] and multivariate curve resolution [26] have also been demonstrated in the literature

Table 2. Correlation Table for Sample Set #1: NESTT—TNT, RDX, PETN, and Potassium Nitrate

Reference Sample	Band 1	Band 2	Test Samples			
			TNT	RDX	PETN	Potassium Nitrate
TNT	2200–2600	3200–3500	1.00	0.47	0.05	0.01
RDX	2200–2600	3200–3500	0.47	1.00	−0.05	−0.33
PETN	2200–2600	3200–3500	0.05	−0.05	1.00	0.03
Potassium Nitrate	3500–3700	—	−0.81	−0.46	−0.38	1.00

Table 3. Correlation Table for Sample Set #2: Ammonium Nitrate, Urea, Gypsum, and Pine Wood

Reference Sample	Band 1	Band 2	Test Samples			
			Ammonium Nitrate	Urea	Gypsum	Pine Wood
Ammonium Nitrate	1400–1770	1780–2470	1.00	0.34	−0.25	0.24
Urea	1340–1620	3980–4150	−0.24	1.00	0.15	0.67
Gypsum	1820–2070	3730–4070	−0.16	−0.23	1.00	−0.11
Pine Wood	1300–1840	1850–2200	0.62	0.67	0.39	1.00

Table 4. Correlation Table for Sample Set #3: Military CARC-Green and Automotive Black, Red, and Green Paints

Reference Sample	Band 1	Band 2	Test Sample			
			CARC-Green	Auto-Black	Auto-Red	Auto-Green
CARC-green	1200–1850	2850–3150	1.00	0.21	−0.27	0.17

for the detection of trace amounts in the presence of interfering species.

5. Discussion

The limitations and scope for further improvement of the different aspects of the SC-based diffuse reflection spectroscopy technique are discussed in this section.

A. Signal-to-Noise Ratio of Reflection Measurements

We begin by performing a detailed signal-to-noise ratio (SNR) estimate of our system, which determines the smallest relative percentage change in sample reflectivity that can be measured at a given standoff distance. The signal voltage measured at the lock-in amplifier can be computed by determining the power reaching the InSb detector after diffuse reflection from the sample. Our analysis assumes a detection wavelength of 4000 nm and a sample reflectivity of 10%. First, the SC output spectral power density at the detection wavelength is determined from Fig. 3 in Subsection 2.B. Next, the power density reaching the sample is calculated after reflection from the collimating mirror, transmission through the chopper, and a second reflection from the turn mirror next to the sample. Assuming the sample to be a Lambertian reflector, the amount of light captured by the concave collection mirror placed a given distance from the sample can also be calculated. Finally, after taking into account the grating efficiency and the monochromator output slit bandwidth, the power incident on the detector can be determined. The voltage signal on the lock-in amplifier is calculated by multiplying the optical power incident on the detector with the detector responsivity, followed by the transimpedance gain of the preamplifier. Using the actual values of the various terms in our system, the analysis is performed below.

Detection wavelength, $\lambda = 4000$ nm (assumption)
SC spectral power density, $P_{SC} = 1$ mW/nm
Mirror 1 reflection, $R_{m1} = 95\%$
Chopper transmission, $T_{ch} = 50\%$
Mirror 2 reflection, $R_{m2} = 95\%$
Sample reflectivity, $R_s = 10\%$ (assumption)
Sample to collection mirror distance, d (variable parameter)
Collection mirror radius, $r = 6$ cm
Spectrometer output slit bandwidth, $\Delta\lambda = 10.8$ nm
Grating efficiency, $\eta = 27\%$
InSb detector responsivity, $D = 1.9$ A/W
Preamp transimpedance gain, $G = 1.07 \times 10^5$ V/A.

Signal voltage measured at the lock-in amplifier:

$$V_{\text{signal}} = P_{SC} \times R_{m1} \times T_{ch} \times R_{m2} \times R_s \times (\pi/d^2) \times (\pi r^2) \times \Delta\lambda \times \eta \times D \times G = 0.096/d^2. \quad (1)$$

The total noise floor of the measurement is a combination of the detector noise, SC fluctuations, preamplifier noise, and lock-in amplifier noise. Because each noise term is independent, the total noise can be computed from the square root of the sum of the squares of the various terms. The detector noise term is calculated by multiplying the shot noise current

density (from the dark current) with the transimpedance gain of the preamplifier. As was shown in Subsection 3.D, the SC fluctuations are proportional to the SC output power. Thus, the noise term can be modeled as a fixed root-mean-square percentage fluctuation with respect to a mean signal level. Finally, we also include contributions to the noise from the transimpedance preamplifier and lock-in amplifier voltage noise. However, we will show later that the last two terms are much smaller compared to the detector and SC noise. Hence, they can be neglected for further analysis. After computing the total voltage noise density, the total voltage noise in the measurements is calculated by multiplying the noise density with the square root of the detection bandwidth (as set by the lock-in amplifier).

Using the generalized equations (1)–(6), the predicted variation of the SNR with sample distance is shown in Fig. 12. The top curve is calculated for the actual experimental noise bandwidth of 1 Hz, while the middle and bottom curves are for higher noise bandwidths of 10 Hz and 100 Hz, corresponding to smaller lock-in time constants of 10 and 1 ms, respectively. We observe that the curves have two different shapes in two distinct regions. At sample distances below 10 m, the curve is flat, corresponding to the limiting case 1. We observe a constant SNR ~ 28, 23, and 18 dB, respectively, for the top, middle, and bottom curves. We call this region the SC fluctuation noise limited region. However, at longer distances corresponding to case 2, there is a constant drop in the SNR with increasing distance. In this region,

$$\begin{aligned}&\text{InSb detector dark current, } I_{\text{det}} = 36\ \mu\text{A (manufacturer spec)}\\&\text{Detector dark current shot noise current density, } I_{\text{det}} = (2eI_{\text{det}})^{1/2}\ \text{pA/Hz}^{1/2}\\&\text{Detector dark current shot noise voltage density, } e_{\text{det}} = i_{\text{det}} \times G = 363\ \text{nV/Hz}^{1/2}\end{aligned} \tag{2}$$

$$\text{SC noise density, } e_{\text{SC}} = 0.0016 * V_{\text{signal}}\ \text{nV/Hz}^{1/2}\ \text{(from Subsection 3.D)} \tag{3}$$

$$\begin{aligned}&\text{Lock-in amplifier noise, } e_{\text{lia}} = 7\ \text{nV/Hz}^{1/2}\ \text{(manufacturer spec)}\\&\text{Detector preamp noise, } e_{\text{pa}} = 20\ \text{nV/Hz}^{1/2}\ \text{(manufacturer spec)}\\&\text{Total noise floor density, } e_{\text{tot}} = \left(e_{\text{det}}^2 + e_{\text{SC}}^2 + e_{\text{lia}}^2 + e_{\text{SC}}^2\right) \sim \left(e_{\text{det}}^2 + e_{\text{SC}}^2\right)^{1/2}\end{aligned} \tag{4}$$

$$\begin{aligned}&\text{Lock-in detection bandwidth, } B = 1\ \text{Hz}\\&\text{Total noise floor, } V_{\text{noise}} = e_{\text{tot}} \times B^{1/2}\end{aligned} \tag{5}$$

$$\begin{aligned}\text{SNR(linear)} &= V_{\text{signal}}/V_{\text{noise}}\\ \text{SNR(dB)} &= 10 \times \log(V_{\text{signal}}/V_{\text{noise}}).\end{aligned} \tag{6}$$

The SNR equation can be further simplified for two limiting cases. At a critical sample distance $d_c \sim 20.5$ m, $e_{\text{SC}} = e_{\text{det}}$—using Eqs. (1), (2), and (3).

Case 1: At distances $d \ll d_c$, $e_{\text{SC}} \gg e_{\text{det}}$, and $e_{\text{tot}} \sim e_{\text{SC}}$.
Thus, SNR $= V_{\text{signal}}/(0.0016\ V_{\text{signal}}) = 625 = 28$ dB (constant).

Case 2: At distances $d \gg d_c$, $e_{\text{det}} \gg e_{\text{SC}}$, and $e_{\text{tot}} \sim e_{\text{det}}$.
Thus, SNR $= (0.096/d^2)/(363e-9) = 2.6e5/d^2$ (inversely proportional to the square of the sample distance).

the SNR is detector noise limited and the SNR falls by 6 dB for every doubling of the sample distance.

Finally, we verify the calculations by experimentally measuring the SNR at different distances and comparing it to the predicted value. At a wavelength of 4000 nm, the reflected signal from a 10% reflectivity sample is acquired for a period of 5 min, and the ratio of the mean to standard deviation is defined as the SNR. The available space in our lab limited the maximum sample distance to 5 m. The effect of a longer sample distances is emulated by keeping the sample at the maximum physical distance of 5 m and adjusting an aperture opening in front of the collection mirror to reduce the collected light by the required $1/d^2$ factor. The experimentally measured results for a 1 Hz noise bandwidth are plotted using square markers in Fig. 10, and they are found to be in good agreement with the theoretically predicted curve. Future improvements in the short distance SNR might be accomplished using a ratiometric dual-beam detection scheme [27] to

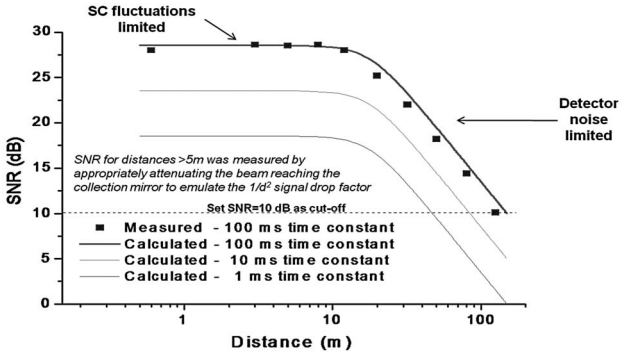

Fig. 12. Variation in predicted system SNR versus sample stand-off distance. At small distances <10 m, the noise is dominated by the SC fluctuations and the SNR is independent of distance. At large distances >20 m, the detector noise term is dominant and SNR is inversely proportional to the square of the sample distance.

reduce the effect of the SC fluctuations, and achieve detector noise limited performance. Another noise term that we have not accounted for is the noise due to beam motion and sample nonuniformity. Because our setup was mounted on a vibration-free optical table, we did not observe any changes in spectrum due to the relative movement of the beam with respect to the sample surface. However, further work needs to be performed to determine the effect of motion on a field portable system with much larger stand-off
distances.

B. System Sensitivity

The system sensitivity for a given SNR is defined as being equal to the minimum band depth (Fig. 13) that can be measured. Under the assumption that a band depth ~3 standard deviations above the noise floor can be measured, the system sensitivity expressed as a percentage is equal to 300/SNR. As an example, the SNR at 5 m is 625, corresponding to a system sensitivity of 0.48%. Assuming a cut-off value of SNR = 10 dB (minimum band depth of 30%), our current system can be used to make

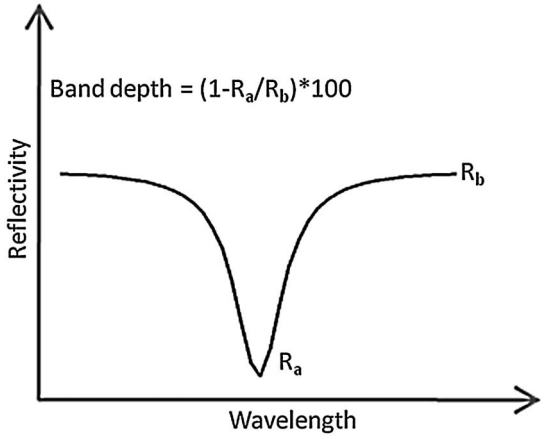

Fig. 13. Definition of absorption band depth. R_a is the reflectance value at the bottom of an absorption dip, while R_b is the reflectance value outside it.

measurements up to a distance of 150 m. If the time constant is reduced from 100 ms (1 Hz noise bandwidth) to 10 ms (10 Hz bandwidth) or 1 ms (100 Hz noise bandwidth), the distance is reduced to 85 or 45 m, respectively, according to Fig. 12. The system sensitivity at large distances can be improved using two methods. First, as discussed earlier in Subsection 2.B, the SC output power may be scaled up further using higher 976 nm pump power and a corresponding increase in pulse repetition rate. Second, because the noise equivalent power for a photodiode is directly proportional to the square root of the active area, the detector noise contribution may be reduced by choosing a detector with a smaller area.

C. System Selectivity

The selectivity of a system is defined as the ability to distinguish between various samples based on their spectral signatures. The conventional "fingerprint" region of a sample is defined as 6.5 to 25 μm, as it contains many of the strong fundamental bending and stretching vibrations. However, we have shown in Section 3 that the SC spectral coverage from 1.2 to 4.2 μm also contains unique spectral features due to various overtone, combination, and fundamental bands. The selectivity of the system was demonstrated in Section 4, where the correlation-function-based algorithm was used to quantitatively demonstrate the dissimilarity between different samples using bands within the 3000 nm wide reflection spectra.

In this paper, we have demonstrated the measurement of the reflectance spectrum of pure samples or those diluted in high concentrations (4%–8%) in a nonabsorbing matrix. However, further research needs to be performed on the detection of trace amounts of relevant samples mixed with other samples to determine the selectivity of the technique in the presence of interfering species. We believe that an improvement in the system selectivity may be achieved by using a light source with a wider spectral bandwidth that covers more absorption features of a sample. An SC source using a 2 cm long fluoride fiber has recently been demonstrated with a spectrum extending to 6.3 μm and average output power of ~20 mW [28]. While the above light source might increase system selectivity due to the wider bandwidth, it would also produce a decrease in system sensitivity due to the lower output power.

D. Acquisition Time

The feasibility of using a stand-off technique in a real-world field application is strongly dependent on the data acquisition time. Because the lock-in amplifier time constant in our setup is 100 ms, the acquisition time should ideally only be ~0.5 s (five time constants for the signal to settle). However, the need to rotate the grating and step through each wavelength means that a complete scan from 1200 to 4200 nm takes ~150 s (300 data points 10 nm apart). The replacement of the current scanning

monochromator with a linear detector array spectrograph would reduce the acquisition time by over 2 orders of magnitude by measuring the entire spectrum in a single shot. By averaging N such shots, the SNR of the measurements can be improved by a factor of $N^{1/2}$. Spectrographs for the visible and near-IR regions using silicon and InGaAs arrays are widely commercially available. However, the high cost of manufacturing of mid-IR arrays has kept their use largely limited to the defense and astronomical imaging communities [29].

E. Comparison with Other Optical Stand-Off Techniques

In this section, we summarize the various performance metrics of our system and provide a comparison with other optical stand-off detection techniques. A recent review by Wallin *et al.* [30] on laser-based stand-off detection of explosives features a comparison table of different optical techniques. Table 5 has been adapted from the above publication, and an additional row with our SC-based diffused reflection spectroscopy system has been added to the top. The different techniques are compared on the basis of sensitivity, selectivity, sensitivity to interferents, stand-off distance, detection time, and system complexity.

Based on the analysis in Subsections 5.A and 5.B, we can claim the SC-based diffuse reflection spectroscopy technique as having "high" sensitivity due to the high output power of the SC source combined with the low noise detection scheme. However, like all the other techniques, the system sensitivity decreases with increasing distance for a constant detection time. We have listed the stand-off distance as 150 m because the SNR drops below the cut-off value of 10 dB at larger distances. In terms of selectivity, the SC-based diffuse reflection spectroscopy technique is inferior compared to the Raman-based techniques, and it is hence listed as "medium." Because the SC spectrum does not cover the conventional molecular vibration fingerprint region of the spectrum beyond 6 μm, we are limited to identifying samples based on the weaker overtone and combination bands or a limited number of fundamental vibration bands associated with the constituent functional groups. In comparison, the Raman spectroscopy methods usually measure the entire Raman spectral range of ~3800 cm^{-1} containing very unique fingerprints for each sample. Thus, they provide high selectivity, but often at the cost of increased system complexity.

The sensitivity to interferents is closely related to the selectivity of the technique. We expect our technique to detect trace amounts of a substance in the presence of interfering species, provided the absorption feature of the target sample has a strong absorption cross section in a wavelength region where the interfering species does not absorb strongly [31]. However, because we have not experimentally measured the reflection spectra under these conditions, this field in the comparison table has been left blank. Finally, in the detection time column, we have listed the value for our technique as 150 s. From a fundamental SNR standpoint, the demonstrated light source has enough output power to perform a sample reflectance measurement in just 0.5 s. However, as discussed earlier, a complete sample scan in our setup takes ~150 s due to a limitation of the scanning monochromator instrument.

6. Summary

We measured the diffuse reflection spectrum from 1200 to 4200 nm of various solid samples at a stand-off distance of 5 m, using a mid-IR SC light source with 3.9 W average output power and spectrum spanning 750 to 4300 nm. The SC source was generated by pumping a 9 m long, 8 μm core diameter, and 0.27 NA ZBLAN fluoride fiber with ~19 kW peak power pulses at 1543 nm from a dual-stage cladding pumped Er-Yb fiber amplifier system. The SC average output power was linearly scalable with the 976 nm power-amplifier pump power, and the highest demonstrated output was only limited by the available pump power.

The first sample set comprised NESTT explosives containing between 4%–8% of TNT, RDX, PETN, and potassium nitrate on a fused silica substrate. The second sample set consisted of ammonium nitrate, urea, gypsum, and pine wood, while the third sample set was made of aluminum blocks painted with automotive and military CARC paint. For each sample, we observed unique spectral features in the reflection spectrum, attributed to the fundamental and overtone vibration frequencies of the various molecular bonds in the sample structure. A correlation-function-based algorithm was used to demonstrate

Table 5. Comparison of Spectroscopic Optical Stand-Off Detection Techniques (Adapted from Wallin *et al.* [7])[a]

Method	Sensitivity	Molecular Selectivity	Sensitivity to Interferents	Distance (m)	Detection Time (s)	Complexity
SC-based DRS	High	Medium	NA	~150	~150	Low
LIBS	High	Medium	Medium to high	>45	~1	Low to medium
Raman spectroscopy	Medium	High	Low to medium	470	~1	Low
RRS	High	Very high	Low	>30	~10	Medium
CARS	Very high	High	Low	>12	~10	Very high
PF-LIF	Medium	Medium	Medium	~30	~1	Medium

[a]SC DRS, supercontinuum-based diffuse reflection spectroscopy; LIBS, laser-induced breakdown spectroscopy; RRS, resonance Raman spectroscopy; CARS, coherent anti-Stokes Raman spectroscopy; PF-LIF, photofragmentation followed by laser induced fluorescence.

system selectivity by quantifying the dissimilarity between various spectra based on selected spectral features in chosen wavelength bands.

Finally, the variation of the SNR with distance was theoretically calculated, and also verified experimentally. For a time constant of 100 ms corresponding to ~1 Hz noise bandwidth, we obtained a SNR ~625 at distances <10 m. Assuming a minimum detectable SNR ~10, the maximum stand-off distance with the current SC output power and integration time was determined to be ~150 m. Future work on the system may include faster acquisition time using a linear detector array spectrograph and measurement of trace amounts of a sample to determine the sensitivity of the technique to interferents.

We would like to thank our sponsors—Omni Sciences, Inc., the U.S. Army Communications-Electronics Research, Development and Engineering Center (CERDEC, contract no. W15P7T-10-C-H606), the Defense Advanced Research Projects Agency (DARPA), and Naval Air Systems Command (NAVAIR) PMA-272 for their support.

References

1. M. P. Fuller and P. R. Griffiths, "Diffuse reflectance measurements by infrared Fourier transform spectroscopy," Anal. Chem. **50**, 1906–1910 (1978).
2. I. Schneider, G. Nau, T. V. V. King, and I. Aggarwal, "Fiber optic near-infrared reflectance sensor for detection of organics in soils," IEEE Photon. Technol. Lett. **7**, 87–89 (1995).
3. M. Leona and J. Winter, "Fiber optics reflectance spectroscopy: a unique tool for the investigation of Japanese paintings," Studies Conser. **46**, 153–162 (2001).
4. B. I. Vasil'ev and O. M. Mannoun, "IR differential-absorption LIDARs for ecological monitoring of the environment," Quantum Electron. **36**, 801–820 (2006).
5. G. Comanescu, C. K. Manka, J. Grun, S. Nikitin, and D. Zabetakis, "Identification of explosives with two-dimensional ultraviolet resonance Raman spectroscopy," Appl. Spectrosc. **62**, 833–839 (2008).
6. H. Li, D. A. Harris, B. Xu, P. J. Wrzesinski, V. V. Lozovoy, and M. Dantus, "Standoff and arms-length detection of chemicals with single-beam coherent anti-Stokes Raman scattering," Appl. Opt. **48**, B17–B22 (2009).
7. A. J. Hobro and B. Lendl, "Stand-off Raman spectroscopy," Trends Anal. Chem. **28**, 1235–1242 (2009).
8. J. L. Gottfried, F. C. D. Lucia, Jr., C. A. Munson, and A. W. Miziolek, "Laser induced breakdown spectroscopy for detection of explosives residues: a review of recent advances, challenges and future prospects," Anal. Bionanal. Chem. **395**, 283–300 (2009).
9. V. Swayambunathan, G. Singh, and R. C. Sausa, "Laser photofragmentation-fragment detection and pyrolysis-laser-induced fluorescence studies on energetic materials," Appl. Opt. **38**, 6447–6454 (1999).
10. R. Furstenberg, C. Kendziora, M. Papantonakis, S. V. Stepnowski, J. Stepnowski, V. Nguyen, M. Rake, and R. A. McGill, "Stand-off detection of trace explosives via resonant infrared photothermal imaging," Appl. Phys. Lett. **93**, 224103 (2008).
11. A. Savitzky and M. J. E. Golay, "Smoothing and differentiation of data by simplified least squares procedures," Anal. Chem. **36**, 1627–1639 (1964).
12. C. Xia, M. Kumar, O. P. Kulkarni, M. N. Islam, F. L. Terry, Jr., M. J. Freeman, M. Poulain, and G. Mazé, "Mid-infrared supercontinuum generation to 4.5 μm in ZBLAN fluoride fibers by nanosecond diode pumping," Opt. Lett. **31**, 2553–2555 (2006).
13. M. Kumar, C. Xia, X. Ma, V. V. Alexander, M. N. Islam, F. L. Terry, Jr., C. Aleksoff, A. Klooster, and D. Davidson, "Power adjustable visible supercontinuum generation using amplified nanosecond gains-witched laser diode," Opt. Express **16**, 6194–6201 (2008).
14. J. C. Carter, S. M. Angel, M. Lawrence-Snyder, J. Scaffidi, R. E. Whipple, and J. G. Reynolds, "Standoff detection of high explosive materials at 50 meters in ambient light conditions using a small Raman instrument," Appl. Spectrosc. **59**, 769–775 (2005).
15. S. V. Ingale, P. U. Sastry, A. K. Patra, R. Tewari, P. B. Wagh, and S. C. Gupta, "Micro structural investigations of TNT and PETN incorporated silica xerogels," J. Sol-Gel Sci. Technol. **54**, 238–242 (2010).
16. A. Banas, K. Banas, M. Bahou, H. O. Moser, L. Wen, P. Yang, Z. J. Li, M. Cholewa, S. K. Lim, and Ch. H. Lim, "Post-blast detection of traces of explosives by means of Fourier transform infrared spectroscopy," Vibrat. Spectrosc. **51**, 168–176 (2009).
17. J. Janni, B. D. Gilbert, R. W. Field, and J. I. Steinfeld, "Infrared absorption of explosive molecule vapors," Spectrochim. Acta Part A **53**, 1375–1381 (1997).
18. G. Anbalagan, S. Mukundakumari, K. S. Murugesan, and S. Gunasekaran, "Infrared, optical absorption, and EPR spectroscopc studies on natural gypsum," Vibrat. Spectrosc. **50**, 226–230 (2009).
19. T. Poli, O. Chiantore, M. Nervo, and A. Piccirillo, "Mid-IR fiber-optic reflectance spectroscopy for identifying the finish on wooden furniture," Anal. Bioanal. Chem. **400**, 1161–1171 (2011).
20. C. M. Canal, A. Saleem, R. J. Green, and D. A. Hutchins, "Remote identification of chemicals concealed behind clothing using near infrared spectroscopy," Anal. Meth. **3**, 84–91 (2011).
21. J. E. Stewart, "Infrared absorption spectra of urea, thiourea, and some thiourea-alkali halide complexes," J. Chem. Phys. **26**, 248–255 (1957).
22. Lawrence Berkeley National Laboratory Pigment Database—Cobalt Chromite Green Spinel, http://coolcolors.lbl.gov/LBNL-Pigment-Database/paints/G05.html.
23. P. J. Kaste, R. G. Daniel, R. A. Pesce-Rodriguez, M. A. Schroeder, and J. A. Escarsega, "Hydrogen plasma removal of military paints: chemical characterization of samples," Report no. A128453, Army Research Laboratory, Aberdeen Proving Ground, 1998.
24. F. V. D. Meer and W. Bakker, "CCSM: cross correlogram spectral matching," Int. J. Remote Sensing **18**, 1197–1201 (1997).
25. T. H. Demetriades-Shah, M. D. Steven, and J. A. Clark, "High resolution derivatives spectra in remote sensing," Remote Sens. Environ. **33**, 55–64, 1990.
26. N. B. Gallagher, T. A. Blake, P. L. Gassman, J. M. Shaver, and W. Windig, "Multivariate curve resolution applied to infrared reflection measurements of soil contaminated with an organophosphorus analyte," Appl. Spectrosc. **60**, 713–722 (2006).
27. M. G. Allen, K. L. Carleton, S. J. Davis, W. J. Kessler, C. E. Otis, D. A. Palombo, and D. M. Sonnenfroh, "Ultrasensitive dual-beam absorption and gain spectroscopy: applications for near-infrared and visible diode laser sensors," Appl. Opt. **34**, 3240–3249 (1995).
28. G. Qin, X. Yan, C. Kito, M. Liao, C. Chaudhari, T. Suzuki, and Y. Ohishi, "Ultrabroadband supercontinuum generation from ultraviolet to 6.28 μm in a fluoride fiber," Appl. Phys. Lett. **95**, 161103 (2009).
29. J. T. Rayner, D. W. Toomey, P. M. Onaka, A. J. Denault, W. E. Stahlberger, W. D. Vacca, M. C. Cushing, and S. Wang, "A medium-resolution 0.8–5.5 micron spectrograph and imager for the NASA Infrared Telescope Facility," Publ. Astron. Soc. Pac. **115**, 362–382 (2003).
30. S. Wallin, A. Pettersson, H. Ostmark, and A. Hobro, "Laser based standoff detection of explosives: a critical review," Anal. Bioanal. Chem. **395**, 259–274 (2009).
31. L. A. Averett and P. R. Griffiths, "Mid-infrared diffuse reflection of a strongly absorbing analyte on non-absorbing and absorbing matrices. Part I: Homogeneous powders," Appl. Spectrosc. **62**, 377–382 (2008).